



Publication Year	2019
Acceptance in OA	2020-11-27T11:31:30Z
Title	Supernova remnants in clumpy media: particle propagation and gamma-ray emission
Authors	Silvia Celli, MORLINO, GIOVANNI, Stefano Gabici, Felix Aharonian
Publisher's version (DOI)	10.1093/mnras/stz1425
Handle	http://hdl.handle.net/20.500.12386/28586
Journal	MONTHLY NOTICES OF THE ROYAL ASTRONOMICAL SOCIETY
Volume	487

Supernova remnants in clumpy media: particle propagation and gamma-ray emission

S. Celli¹,¹★ G. Morlino²,^{1,2} S. Gabici³ and F. A. Aharonian^{1,4,5}

¹Gran Sasso Science Institute, Viale Francesco Crispi 7, 67100 L'Aquila, Italy

²INAF, Osservatorio Astrofisico di Arcetri, L.go E. Fermi 5, 50125, Firenze, Italy

³APC, AstroParticule et Cosmologie, Université Paris Diderot, CNRS/IN2P3, CEA/Irfu, Obs. de Paris, Sorbonne Paris Cité, France

⁴Max-Planck-Institut für Kernphysik, Postfach 103980, D-69029 Heidelberg, Germany

⁵Dublin Institute for Advanced Studies, 31 Fitzwilliam Place, Dublin 2, Ireland

Accepted 2019 May 21. Received 2019 May 21; in original form 2018 April 27

ABSTRACT

Observations from the radio to the gamma-ray wavelengths indicate that supernova remnant (SNR) shocks are sites of effective particle acceleration. It has been proposed that the presence of dense clumps in the environment where supernovae explode might have a strong impact on the shape of the hadronic gamma-ray spectrum. Here we present a detailed numerical study of the penetration of relativistic protons into clumps that are engulfed by a SNR shock, taking into account the magneto-hydrodynamical properties of the background plasma. We show that the spectrum of protons inside clumps is much harder than that in the diffuse inter-clump medium, and we discuss the implications for the formation of the spectrum of hadronic gamma-rays, which no longer reflects the acceleration spectrum of protons, resulting substantially modified inside the clumps owing to propagation effects. For the Galactic SNR RX J1713.7 – 3946, we show that a hadronic scenario including dense clumps inside the remnant shell is able to reproduce the broadband gamma-ray spectrum from GeV to TeV energies. Moreover, we argue that small clumps crossed by the shock could provide a natural explanation for the non-thermal X-ray variability observed in some hotspots of RX J1713.7 – 3946. Finally, we discuss the detectability of gamma-ray emission from clumps with the upcoming Cherenkov Telescope Array, and the possible detection of the clumps themselves through molecular lines.

Key words: acceleration of particles – instabilities – radiation mechanisms: non-thermal – shock waves – ISM: supernova remnants – gamma-rays: general.

1 INTRODUCTION

It is now well established that supernova remnants (SNRs) can accelerate electrons and presumably also hadrons, as demonstrated by the non-thermal emission detected from the great majority of SNRs. In particular, the pion-bump detected at ~ 280 MeV from two middle-aged SNRs, IC 443 and W 44, indicates the presence of accelerated hadrons (Ackermann et al. 2013) (but see also Cardillo, Amato & Blasi (2016) for an alternative explanation). Two main questions need to be answered, however, in order to validate the idea that SNRs represent the main source of Galactic cosmic rays (CRs) observed on Earth: what is the total amount of energy channelled into relativistic particles, and what is the final energy spectrum of accelerated particles injected into the interstellar medium (ISM)? Gamma-ray observations provide a powerful tool to answer these questions, allowing us to infer the properties of accelerated hadrons directly.

In some young SNRs it is still unclear whether the detected gamma-ray emission is produced by leptonic processes, via inverse Compton (IC) scattering, or by hadronic collisions, through the decay of the resulting neutral pions. Generally speaking, the two scenarios differ mainly in the required magnetic field strength: the IC scenario usually requires a very low magnetic field (of the order of $10 \mu\text{G}$) in order to simultaneously account for the radio, X-ray and gamma-ray emission, while the hadronic scenario requires much larger values, of the order of few hundreds of microgauss. Such a large magnetic field cannot result from the simple compression of the interstellar magnetic field, but requires some amplification, which is, in turn, a possible signature of efficient CR acceleration. The case of RX J1713.7 – 3946 is of special interest in this respect. This remnant has been considered for a long time to be the best candidate for an efficient acceleration scenario, mainly owing to its high gamma-ray flux. The detection of gamma-ray emission in the energy range $[1\text{--}300]$ GeV by the *Fermi*-LAT satellite (Abdo et al. 2011) showed an unusually hard spectrum, which, at first glance, seems to be in better agreement with a leptonic scenario. However,

* E-mail: silvia.celli@gssi.infn.it

a deeper analysis showed that neither the hadronic nor the leptonic scenario, taken in their simplest form, can unequivocally explain the observations (Morlino, Amato & Blasi 2009a; Zirakashvili & Aharonian 2010; Gabici & Aharonian 2016). To address this issue, it was proposed by Zirakashvili & Aharonian (2010), Inoue et al. (2012) and Gabici & Aharonian (2014) that the very hard energy spectrum at low energies could result from hadronic emission if the SNR were expanding inside a clumpy medium. In the presence of dense inhomogeneities, in fact, the magnetic field can be amplified all round the clump because of both the field compression and the magneto-hydrodynamical (MHD) instabilities that develop in the shock–clump interaction: this makes it difficult for particles at low energies to penetrate inside the clump compared with the most energetic ones. Consequently, the gamma-ray spectrum would be harder than the parent proton spectrum accelerated at the forward shock.

In this work we study the realization of such a scenario. In Section 2, we introduce clumps and describe the interaction between a shock and a clump, examining the temporal and spatial evolution of the background plasma properties through a 3D MHD simulation. Then, in Section 3, we focus on the temporal and spatial evolution of the density of accelerated particles, solving the 3D transport equation for CRs propagating into a clumpy medium where a shock is expanding. The diffusion coefficient around the clump is parametrized in order to reproduce the amplified magnetic field resulting from both the regular field compression and MHD instabilities. Once the behaviour of the particle density is obtained, the CR spectrum inside and outside the clump region is derived, revealing that the spectrum inside the clump is much harder at early epochs and steepens at later times. The same spectral trend is exhibited in the related gamma-ray emission from inelastic proton–proton collisions, as shown in Section 4. In order to move from the gamma-ray emission of individual clumps to their cumulative contribution, we will assume a uniform spatial distribution of clumps. The case of RX J1713.7 – 3946 is then presented in Section 5: in particular, in Section 5.1 we explore the possibility of detecting clumps embedded inside the remnant through molecular lines, while in Section 5.2 we comment on the fast variability observed in non-thermal X-rays. Finally, in Section 5.3, we discuss the detectability of clump–shock associations by the major next-generation, ground-based gamma-ray instrument, the Cherenkov Telescope Array (CTA). We summarize our conclusions in Section 6.

2 SHOCK PROPAGATION THROUGH A CLUMPY MEDIUM

Observations of the ISM have revealed a strong non-homogeneity, particularly inside the Galactic plane. On the scales of the order of few parsecs, dense molecular clouds (MCs) constitute structures mainly composed of H_2 molecules, while their ionized component is composed by C ions. Typical temperatures and masses are of the order of $T_{\text{MC}} \simeq 10^2$ K and $M_{\text{MC}} \gtrsim 10^3 M_{\odot}$. On smaller scales (of the order of a fraction of a parsec), colder and denser molecular clumps are present: they are characterized by typical temperatures of $T_c \simeq 10$ K, masses of the order of $M_c \simeq 0.1\text{--}1 M_{\odot}$, and therefore number densities of the order of $n_c \gtrsim 10^3 \text{ cm}^{-3}$. In the following, we will consider the lower bound as a reference value for the density of the target gas inside individual clumps. These clumps are composed mostly of neutral particles, while the most relevant ions are HCO^+ . Typical values for the ionized density are equal to $n_i \leq 10^{-4} n_c$, while the average mass of ions is $m_i = 29m_p$ (m_p is the proton mass) and that of neutrals is $m_n = 2m_p$. Therefore, the ion-to-neutral mass

density ϵ in clumps amounts to (Gabici & Montmerle 2016)

$$\epsilon = \frac{m_i n_i}{m_n n_n} \leq 1.5 \times 10^{-3} \ll 1. \quad (1)$$

Molecular clouds are strongly influenced by the presence of CRs, because most likely low-energy CRs determine their ionization rate (see Padovani, Galli & Glassgold 2009; Phan, Morlino & Gabici 2018), which in turns controls both the chemistry of clouds and the coupling of plasma with local magnetic fields, and hence star formation processes.

Shocks propagating through inhomogeneities of the ISM are able to generate MHD instabilities, which modify the thermal properties of the plasma and might be able to disrupt the clumps because of thermal conduction (Orlando et al. 2008). Therefore, the dynamical interaction between the shock emitted at the supernova (SN) explosion and the medium surrounding the star is an essential ingredient for an understanding of star formation processes (Hennebelle 2013; Dwarkadas 2007). In particular, the environment where Type II SNe explode is most likely populated by molecular clumps: indeed, given their fast evolution, these SNe explode in an environment rich in molecular clouds, namely the same environment that generated the star. Moreover, given that SNe have a massive progenitor, strong winds in the giant phase of the stars' evolution accelerate the fragmentation of clouds into clumps, while creating a large cavity of hot and rarefied gas around them. The physical size of ISM inhomogeneities results from HD simulations that include interstellar cooling, heating and thermal conduction. Such simulations have been conducted by Inoue et al. (2012), who found that the characteristic length-scale of clumps amounts to $R_c \simeq 0.1$ pc, corresponding to the smallest scale where thermal instability is effective. We fix this scale throughout the paper. This scenario could be similar to the one in which the remnant of RX J1713.7 – 3946 is evolving (Slane et al. 1999). Previous works in this direction (Klein, McKee & Colella 1994) have shown that plasma instabilities arise when the upstream medium is not homogeneous (Giacalone & Jokipii 2007; Fraschetti 2013; Sano et al. 2012). In particular, in the presence of density inhomogeneities, vorticity may develop after the passage of the shock. In such a situation, the Kelvin–Helmoltz instability arises, owing to the velocity shear between the clumps and the surrounding medium, generating a strong enhancement of the local magnetic field. The generated turbulence then cascades to smaller spatial scales through a Kolmogorov-like process (Inoue et al. 2012) on time-scales $\tau_{\text{cascade}} = R_c/v_A \simeq 50$ yr (where the Alfvén speed of MHD waves v_A is computed in a low-density environment such as that of a rarefied cavity). In the next section, using MHD simulations, a simplified scenario is studied in which a single clump much denser than the circumstellar plasma is engulfed by a shock. In such a configuration, two different kinds of processes produce magnetic field amplification. Around the clump, the regular field is compressed and stretched, reaching a strength of up to ~ 10 times the original value, in a layer that is found to be about half of the clump size, namely 0.05 pc, similar to the results obtained by Inoue et al. (2012). This region will be referred to as the *clump magnetic skin*. In addition, in the region behind the clump, turbulence develops, and the associated vorticity further amplifies the magnetic field. It is also shown that if the density contrast between the clump and the surrounding medium is very large, the clump can survive for a long time before evaporating, even longer than the SNR age.

2.1 MHD simulations of the shock–clump interaction

The description of the thermal properties of a classical fluid follows from the solution of the Navier–Stokes equations coupled to the induction equation for the time evolution of the background magnetic field \mathbf{B}_0 . The MHD equations of motion to be solved read, for non-resistive fluids, as

$$\begin{cases} \frac{\partial \rho}{\partial t} + \nabla \cdot (\rho \mathbf{v}) = 0 \\ \frac{\partial \mathbf{v}}{\partial t} + \mathbf{v} \cdot \nabla \mathbf{v} = -\frac{1}{\rho} (\nabla p + \frac{1}{4\pi} (\nabla \times \mathbf{B}_0) \times \mathbf{B}_0) \\ \frac{\partial}{\partial t} \left(\mathcal{E} + \frac{B_0^2}{8\pi} \right) = -\nabla \cdot \left[(\mathcal{E} + p) \mathbf{v} + \frac{1}{4\pi} \mathbf{B}_0 \times (\mathbf{v} \times \mathbf{B}_0) \right] \\ \frac{\partial \mathbf{B}_0}{\partial t} = \nabla \times (\mathbf{v} \times \mathbf{B}_0) \\ \nabla \cdot \mathbf{B}_0 = 0, \end{cases} \quad (2)$$

where ρ is the fluid density, \mathbf{v} is its velocity, p is its pressure, $\mathcal{E} = \rho v^2/2 + p/(\gamma - 1)$ is its kinetic plus internal energy, and γ is its adiabatic index ($\gamma = 5/3$ for an ideal monoatomic non-relativistic gas).

In order to introduce a shock discontinuity, as well as the presence of a clump, a numerical approach has been adopted, though the PLUTO code (see Mignone et al. 2007). The shock–cloud interaction is implemented as one of the possible configurations provided by this code. We are interested in performing a 3D simulation, in Cartesian coordinates. The finite-difference scheme adopted for the solution of equation (2) is based on an unsplit third-order Runge–Kutta algorithm with an adaptive time-step subject to the Courant condition, $C = 0.3$. In order to investigate a situation as similar as possible to that of a high-mass star SN explosion, such as RX J1713.7–3946, in the upstream region we set a low-density medium with $n_{\text{up}} = 10^{-2} \text{ cm}^{-3}$, which is compressed by the shock in the downstream region up to $n_{\text{down}} = 4 \times 10^{-2} \text{ cm}^{-3}$. A strong shock is moving in the direction of the z -axis, with a sonic Mach number $M = v_s/c_s \simeq 37$, as expected for this remnant, given its measured shock speed of $v_s = 4.4 \times 10^8 \text{ cm s}^{-1}$ (Uchiyama et al. 2007) and the upstream temperature of $T = 10^6 \text{ K}$, which is typical for bubbles inflated by stellar winds. A flat-density-profile clump is set in the upstream as the initial condition, with a density as high as $n_c = 10^3 \text{ cm}^{-3}$. Therefore, a density contrast

$$\chi = \frac{n_c}{n_{\text{up}}} = 10^5 \quad (3)$$

is assumed: if the shock speed is $\mathbf{v} = v_s \hat{z}$, the shock propagates inside the clump with a velocity $\mathbf{v}_{s,c} = v_{s,c} \hat{z}$ equal to (Klein et al. 1994 and Inoue et al. 2012)

$$v_{s,c} = \frac{v_s}{\sqrt{\chi}} = 1.4 \times 10^6 \text{ cm s}^{-1}. \quad (4)$$

Boundary conditions are set as outflow in all directions, except for the downstream boundary in the z -direction, where an injection flow is set. We set a uniform grid with size $2 \text{ pc} \times 2 \text{ pc} \times 2 \text{ pc}$ and a spatial resolution of $\Delta x = \Delta y = \Delta z = 0.01 \text{ pc}$. A spherical clump of radius $R_c = 0.1 \text{ pc}$ is located at $x_0 = y_0 = z_0 = 1 \text{ pc}$. All the evolution is followed in the clump reference frame.

In the MHD simulation, the clump is assumed to be fully ionized: this is not the real condition, because molecular clumps are composed mainly by neutrals, as discussed in Section 2. However, while the shock is passing through the ionized part of the clump, the heated ions are able to ionize the neutral part on a time-scale of the order of a few years. This condition allows us to consider the neutral clump as if it were completely ionized. In this process, ions cool down and the pressure drops accordingly, reducing the shock speed to a value given by $v_{s,c}$ (Klein et al. 1994). The time needed

for the shock to cross the clump is the so-called clump crossing time,

$$\tau_{\text{cc}} = \frac{2R_c}{v_{s,c}} \simeq 1.4 \times 10^4 \text{ yr}. \quad (5)$$

It has been shown through both analytical estimates (Klein et al. 1994; Chevalier 1999) and simulations (Orlando et al. 2005, 2008) that the time required for the clump to evaporate is of the order of a few times τ_{cc} . This time-scale is larger than the estimated age of RX J1713.7–3946, which amounts to $T_{\text{SNR}} \simeq 1625 \text{ yr}$.

A magnetic field of intensity $B_0^{\text{up}} = 5 \mu\text{G}$ is set in the region upstream of the shock. We present here a simulation of an oblique shock inclined by 45° with respect to the shock normal. We set $\mathbf{B}_0 = (B_{0x}, 0, B_{0z})$, $B_0^{\text{up}} = 5 \mu\text{G}$ and $B_{0x} = B_{0z}$. We are interested in the evolution of the background plasma for about 300 yr from the first shock–clump interaction, as will be described in Section 4. Within this time interval, results from the MHD simulations are shown in Figs 1, 2, 3 and 4, corresponding to plasma mass density, vorticity ω , magnetic energy density and plasma velocity, respectively. The plasma vorticity is here defined as $\omega = \nabla \times \mathbf{v}$. These results can be summarized as follows.

- (i) The clump maintains its density contrast, although the density distribution tends to become smoother, as seen in Fig. 1.
- (ii) During the whole simulated time, the shock has not yet crossed the clump, as represented by the plasma velocity field lines in Fig. 4(a).
- (iii) The regular magnetic field is wrapped around the clump surface in a region with a typical size of $R_c/2$, as shown in Fig. 3. Comparing Figs 2 and 3, it can be seen that the magnetic field in the clump skin is amplified as a result of compression and stretching owing to the strong vorticity that developed in the plasma. The magnetic amplification is most effective where the vorticity is largest, meaning that the shear amplification is more important than pure compression, as previously pointed out by, for example, Mac Low et al. (1994) and Jones, Ryu & Tregillis (1996).¹ The resulting magnetic field energy density is ~ 100 times higher than in the regular downstream region: the amplification factor obtained directly follows from the simulation set-up, namely from the shock Mach number, which is set in order to reproduce the conditions expected to operate in RX J1713.7–3946. The fact that the magnetic field around the clump is mainly directed along the tangential direction implies that it is difficult for accelerated particles to diffuse orthogonally to the clump surface, along the radial direction, as will be discussed in Section 3.3.
- (iv) In the region immediately behind the clump, a long tail is formed, where the plasma develops eddies and will eventually become turbulent, as observed in Fig. 4(a). Also in this region, the magnetic field is amplified up to a factor of ~ 10 . The tail behind the clump is not particularly relevant for the CR propagation inside the clump, but it can be important when considering the synchrotron X-ray emission from electrons (see Section 5.2).

¹In the context of the present work, it is important to stress that we do not see any turbulence developing in the clump skin. Vorticity stream and magnetic field lines are regular in the sense that they do not show eddies; the vorticity observed is due only to the shear. As a consequence, our simulations do not support the idea that a turbulent cascade develops all around the clump surface. On the other hand, it is also possible that some turbulence develops on scales much smaller than our resolution scale.

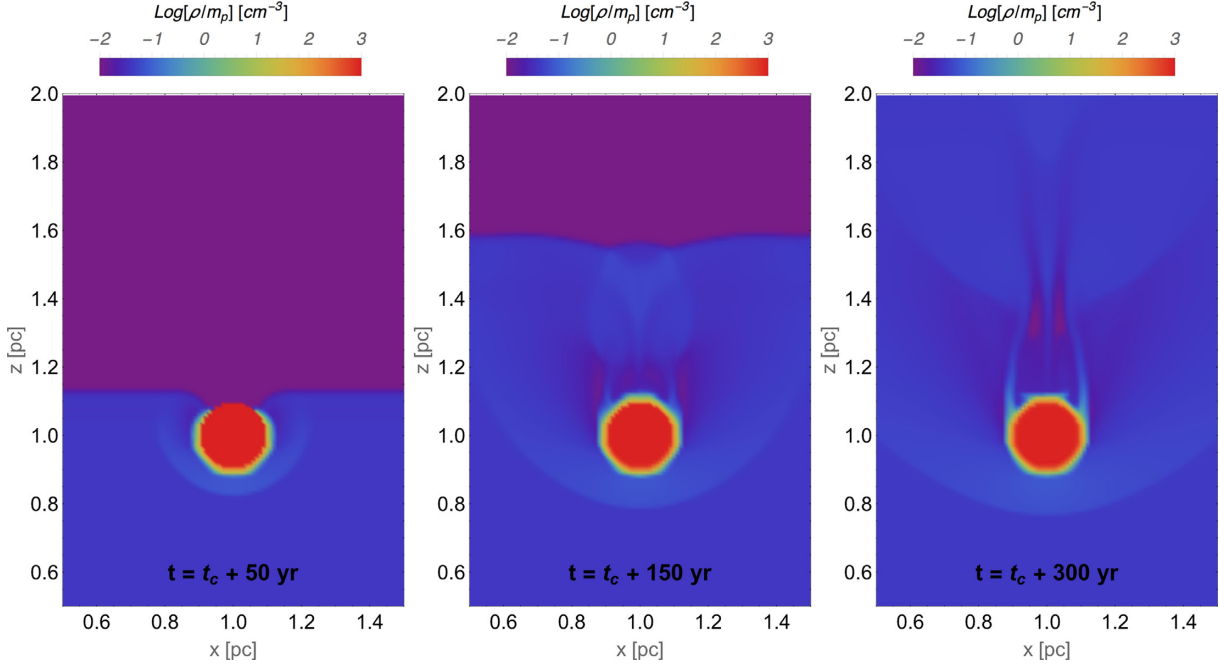


Figure 1. Mass density of the plasma for the 3D MHD simulation in the oblique shock configuration with density contrast $\chi = 10^5$. The plots show a 2D section along $y = 1$ pc, passing through the centre of the clump. From left to right, the evolution is shown for 50, 150 and 300 yr after the first shock–clump contact, occurring at $t = t_c$.

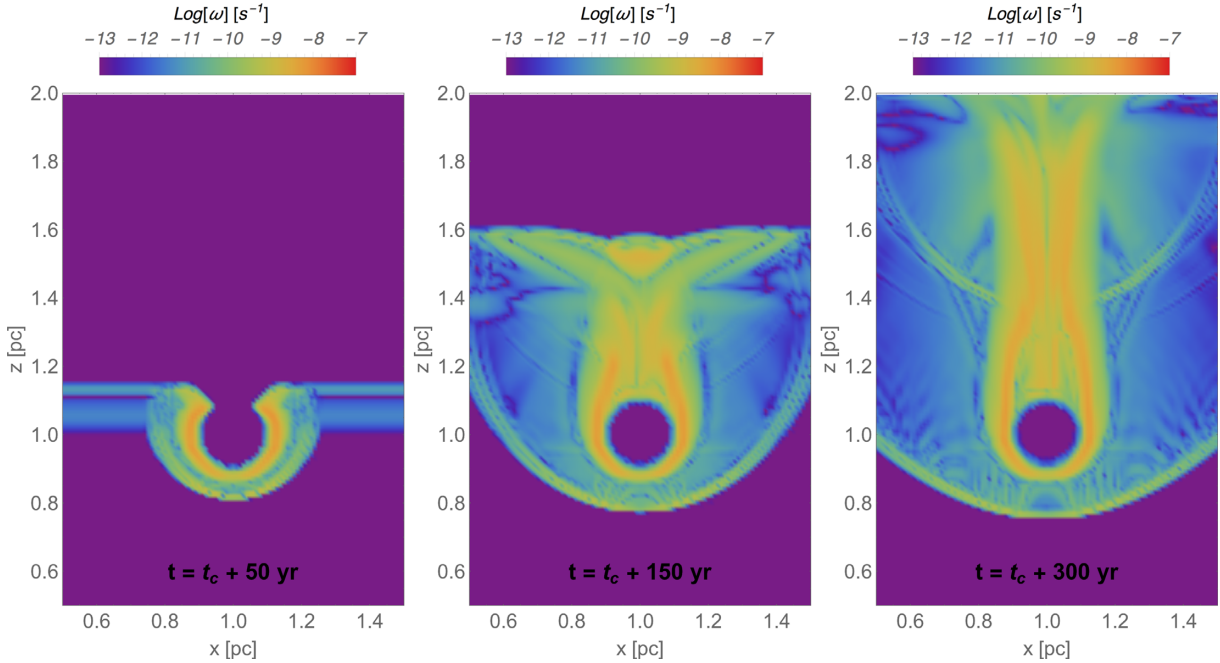


Figure 2. Vorticity $\omega = \nabla \times v$ of the plasma for the same simulation as shown in Fig. 1.

In order to understand whether the magnetic amplification is peculiar to our chosen configuration, we also performed MHD simulations for different values of the initial magnetic field orientation and the density contrast. Concerning the orientation, the only case in which the amplification is negligible is when the magnetic field is purely parallel to the shock normal: in this situation, the magnetic field around the clump is not compressed and the shear is less

effective, while amplification in the tail is observed as a result of plasma vorticity. In order to explore, instead, the effect of the density contrast, we performed simulations with $\chi = 10^2$, 10^3 and 10^4 . In these cases, for a fixed shock speed, we expect the clump to evaporate on shorter time-scales than the one given by equation (5). We found that an effective amplification of the magnetic field around the clump is obtained if $\chi \gtrsim 10^3$. For less massive clumps,

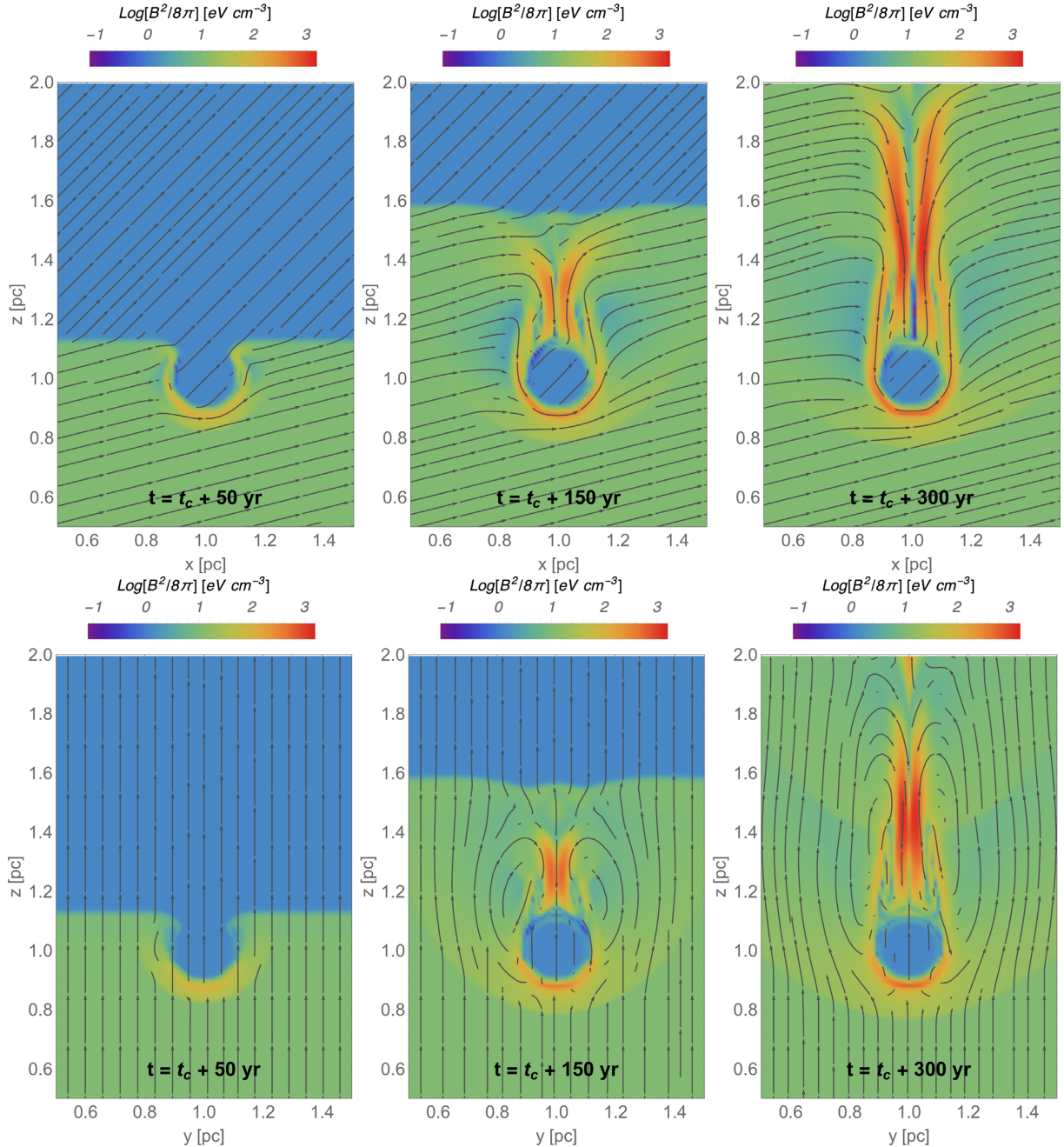


Figure 3. Energy density of the magnetic field (colour scale) for the same simulation as shown in Fig. 1. Upper and lower panels refer to a 2D cut across the centre of the clump in the x - z and y - z planes, respectively, at $y = 1$ pc and $x = 1$ pc, and the stream lines show the direction of the regular magnetic field in the corresponding planes.

where the evaporation time is comparable to the remnant age, two differences arise: (i) once heated, these clumps would contribute to the thermal emission of the remnant; and (ii) the resulting gamma-ray spectrum would not manifest a pronounced hardening. Hence, detailed spectroscopic and morphological observations are crucial for providing a lower limit on the density contrast of the circumstellar medium (CSM). A scenario in which the SNR shock might be accelerating particles into a cloudy ISM with a density contrast as low as $\chi = 10^2$ was considered in Berezhko, Ksenofontov & Völk (2013) to explain the soft spectrum observed in the Tycho's SNR.

3 PARTICLE TRANSPORT

3.1 Transport equation

CRs are scattered by MHD waves parallel to the background magnetic field. The transport equation that describes the temporal and spatial evolution of the CR density function in the phase space $f(\mathbf{x}, \mathbf{p}, t)$ reads as (Ginzburg & Syrovatsky 1961 and Drury 1983)

$$\frac{\partial f}{\partial t} + \mathbf{v} \cdot \nabla f = \nabla \cdot [D \nabla f] + \frac{1}{3} p \frac{\partial f}{\partial p} \nabla \cdot \mathbf{v} + Q_{\text{CR}}, \quad (6)$$

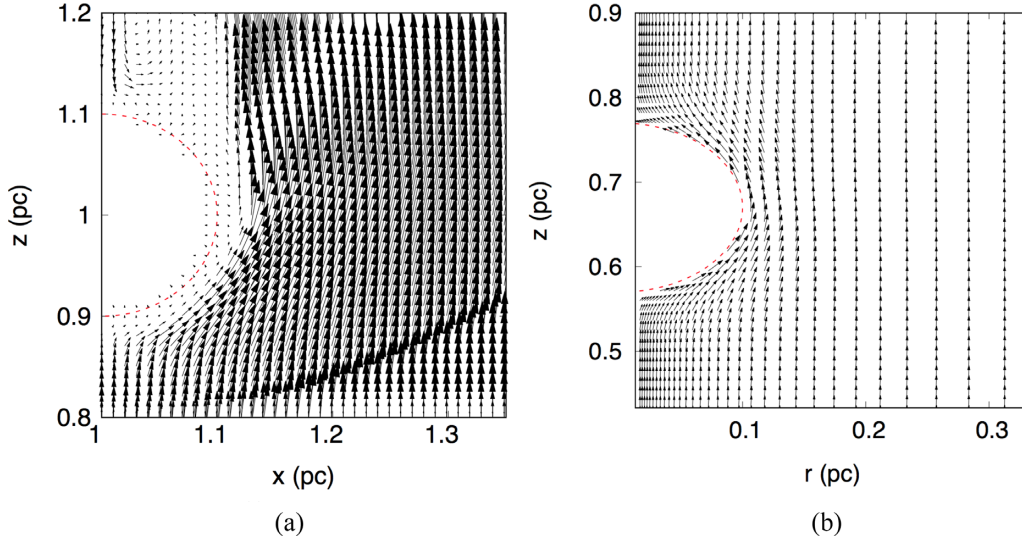


Figure 4. (a) Velocity field resulting from the MHD simulation in the oblique shock configuration with density contrast $\chi = 10^5$, at a time $t = t_c + 300$ yr and in a 2D section along $y = 1$ pc, passing through the centre of the clump. The bow-shock produced by the clump in the shocked ISM is also visible, but is always very mild ($M_2 < 2$). (b) Analytical velocity field adopted in the numerical solution of the transport equation, fully tangential to the clump surface and directed along the z -direction in the far-field limit. The red dashed line defines the clump size, without considering its magnetic skin.

where D is the diffusion coefficient, p is the particle momentum, and $Q_{\text{CR}} = f_{\text{inj}} v_s \delta(z - z_s)$ is the injection flux, assumed to take place at the shock, namely at $z = z_s$. Advection in the background velocity field is expressed by the left-hand side of equation (6), together with the time variation of the particle density function, while diffusion, plasma adiabatic compression and injection are expressed on the right-hand side. Given the system symmetry, we will solve this equation in cylindrical coordinates, through a finite-difference method. A grid of $2 \text{ pc} \times 2 \text{ pc}$ is set, with a spherical clump located at $(r_0, z_0) = (0, 0.67)$ pc. A logarithmic step is used in the radial dimension, while a uniform spacing is fixed along the shock direction. The spatial resolution of the grid is set in such a way that, for each simulated momentum, the proton energy spectrum reaches a convergence level better than 5 per cent. We set an operator splitting scheme based on the alternated direction implicit (ADI) method, flux conservative and upwind, second order in both time and space, subject to a Courant condition $C = 0.8$. The initial condition of the simulation includes the presence of a shock precursor in the upstream region (everywhere but inside the clump, which starts empty of CRs): it represents the equilibrium solution of the diffusive-advective transport equation, such that

$$f(r, z, p, t = 0) = f_0(p) \exp \left[-\frac{(z - z_s) v_s}{D(p)} \right]. \quad (7)$$

Here, $f_0(p)$ represents the particle spectrum at the shock location z_s . We set a p^{-4} power-law spectrum, following the test-particle approach of diffusive shock acceleration (DSA) theory (see Skilling 1975; Bell 1978; Blanford & Ostriker 1978). We added an exponential cut-off in momentum p_{cut} in order to take into account the maximum attainable energy, resulting in

$$f_0(p) \propto p^{-4} \exp \left[-\frac{p}{p_{\text{cut}}} \right]. \quad (8)$$

Boundary conditions are such that a null diffusive flux is set on every boundary, except upstream in the z -direction, where the precursor shape is set.

When the forward shock hits the clump, we assume that the transmitted shock does not accelerate particles because it is very

slow and is propagating in a highly neutral medium. Moreover, we neglect the reflected shock, which propagates back into the remnant, because it would not contribute to the acceleration of particles because of its low Mach number, $M_2 \lesssim 2$. Given the results in Section 2.1, we set an analytical velocity field, irrotational and divergence-less through all the space (except at the shock and clump surface). This is obtained by solving the Laplace equation in cylindrical coordinates for the velocity potential, with the boundary conditions that in the far-field limit the downstream velocity field is directed along the shock direction and equal to $\mathbf{v} = v_{\text{down}} \hat{z} = \frac{3}{4} v_s \hat{z}$, while at the clump surface the field is fully tangential. The resulting solution reads as

$$\begin{cases} v_r(r, z) = -\frac{3}{2} \frac{R_c^3 r z}{(r^2 + z^2)^{5/2}} v_{\text{down}} \\ v_z(r, z) = \left[1 + \frac{1}{2} R_c^3 \frac{(r^2 - 2z^2)}{(r^2 + z^2)^{5/2}} \right] v_{\text{down}}. \end{cases} \quad (9)$$

With such a choice of the velocity field, the adiabatic compression term vanishes. Moreover, we set a null velocity field inside the clump, because $v_{s,c} \ll v_s$, and in the upstream region. A schematic view of the velocity vector field adopted is given in Fig. 4(b). Comparing it with the results from the MHD simulation obtained in Section 2.1 and shown in Fig. 4(a), it can be seen that the two velocity profiles are quite similar, except for the turbulent region behind the clump.

Furthermore, we will consider a stationary, space-dependent and isotropic Bohm diffusion through all the space, so that

$$D_{\text{Bohm}}(\mathbf{x}, p) = \frac{1}{3} r_L(\mathbf{x}, p) v(p) = \frac{1}{3} \frac{pc}{Ze B_0(\mathbf{x})} v(p), \quad (10)$$

where $r_L(\mathbf{x}, p)$ is the Larmor radius of a particle with charge Ze in a background magnetic field $B_0(\mathbf{x})$. In the following we will only consider relativistic protons, with momenta $p \in [1 \text{ GeV}/c - 1 \text{ PeV}/c]$, because this is the energy interval relevant for the production of high-energy and very-high-energy gamma-rays. We set a space-dependent magnetic field $B_0(\mathbf{x})$, defining four regions in the space:

- i) the unshocked CSM;
- ii) the shocked CSM, where $B_0 \equiv B_{\text{CSM}} = 10 \mu\text{G}$;

- iii) the clump interior, with a size of $R_c = 0.1$ pc, where diffusion is not efficient such that $B_0 \equiv B_c = 1 \mu\text{G}$;
- iv) the clump skin, with a size of $R_s = 0.5R_c$ around the clump itself, where the amplification of the magnetic field is realized such that $B_0 \equiv B_s = 100 \mu\text{G}$.

The density profile of accelerated particles diffusing in the region of interaction between the shock and the clump is shown in Figs 5(a), (b) and (c) for particles of different energy. The distribution function is flat in the downstream region, while a precursor starts at the shock position, as defined in equation (7). As expected, low-energy particles penetrate into the clump at much later times with respect to high-energy ones. The time evolution of the CR distribution function for different CR momenta is shown in Fig. 6: Figs 6(a), (c) and (e) refer to 10-GeV particles, while Figs 6(b), (d) and (f) refer to 10-TeV particles. It is apparent that low-energy particles are not able to fill the clump interior uniformly on the temporal scale relevant for the gamma-ray emission (around a few hundred years, as discussed in Section 4).

Note that the value of B_c used above is smaller than the strength of the large-scale magnetic field expected in molecular clouds. We chose such a smaller value as representative of the effective turbulent magnetic field, which determines the diffusion coefficient in equation (10), and is damped by the presence of the ion–neutral friction (see Section 3.2).

The diffusion coefficient in the shock region should be close to the Bohm regime in order to obtain an effective acceleration of protons to multi-TeV energies. For this reason, in equation (10) we assumed isotropic diffusion with $\delta B \simeq B_0$. From a theoretical point of view, such a low diffusion is justified by the self-generation of waves from accelerated particles. Nevertheless, the correct description of the diffusion in the skin region of the clump is not a trivial task. In particular, it is not guaranteed that the turbulent component of the field is also amplified at a level such that Bohm diffusion still applies. In resolving the transport equation, equation (6), we assume that this is indeed the case, namely $\delta B_s \simeq B_s$. However, if the amplification of the turbulence does not occur at the same level, and $\delta B_s < B_s$, the large-scale magnetic field dominates and we can envision two opposite scenarios: (a) the case where magnetic field lines penetrate the clump (which occurs for a small portion of the clump surface located at the back of the cloud, where the magnetic tail develops, as shown in Fig. 3), and (b) the case where these lines stay parallel to the clump surface. While in the former case the relevant diffusion coefficient for particles to penetrate the clump is that parallel to the magnetic field lines, in the latter we need to account for perpendicular diffusion as well. In Sections 3.2 and 3.3 we discuss these two scenarios separately, showing that in both cases the effective D is reduced with respect to the plain downstream.

3.2 Growth and damping of MHD waves

In the following, we investigate the effect of the streaming instability on the amplification of the turbulent magnetic field, as it might significantly contribute to the CR scattering, especially along the magnetic field lines penetrating the clump. In the framework of the non-linear theory of DSA, CRs themselves generate the MHD waves, that the waves are needed to scatter off from one side to the other of the shock surface. If this process occurs in resonant conditions, a CR particle of momentum p is able to excite only magnetic waves of wavenumber $k_{\text{res}} = 1/r_L(p)$. The wave growth is then caused by the streaming of CRs. Thus the CR density, obtained

as a solution of equation (6), affects the amount of turbulence that is generated, which in turn modifies the diffusion properties of the system as (Skilling 1971)

$$D(\mathbf{x}, p, t) = \frac{1}{3} r_L(p) v(p) \frac{1}{\mathcal{F}(k_{\text{res}}, \mathbf{x}, t)}, \quad (11)$$

where $\mathcal{F}(k, \mathbf{x}, t)$ is the turbulent magnetic energy density per unit logarithmic bandwidth of waves with wavenumber k , normalized to the background magnetic energy density as

$$\left(\frac{\delta B(\mathbf{x}, t)}{B_0} \right)^2 = \int \mathcal{F}(k, \mathbf{x}, t) d \ln k. \quad (12)$$

Given the strong non-linearity of the problem, it is computationally prohibitive to solve in a self-consistent way the system composed by the transport equation and by the time evolution of the wave power density, which satisfies the following equation:

$$\frac{\partial \mathcal{F}}{\partial t} + \mathbf{v}_A \cdot \nabla \mathcal{F} = (\Gamma_{\text{CR}} - \Gamma_{\text{D}}) \mathcal{F}, \quad (13)$$

where Γ_{CR} is the growth rate of MHD waves, Γ_{D} is the damping rate, and v_A is the Alfvén speed equal to

$$v_A = \frac{B_0}{\sqrt{4\pi n_i m_i}}. \quad (14)$$

We will, instead, solve equation (6) in a stationary given magnetic field, and, once f is known, we will evaluate a posteriori the contribution of the growth and damping of resonant waves due to CR streaming.

The growth rate of the streaming instability strongly depends on the CR density gradient. We therefore expect it to be more pronounced in the clump skin, where magnetic field amplification makes diffusion very efficient, thus increasing the CR confinement time in this region. The rate can be expressed as (Skilling 1971)

$$\Gamma_{\text{CR}}(k) = \frac{16}{3} \pi^2 \frac{v_A}{B_0^2 \mathcal{F}(k)} [p^4 v(p) \nabla f]_{p=p_{\text{res}}}, \quad (15)$$

where p_{res} represents the resonant momentum. The amplified magnetic field can in turn be damped by non-linear damping (NLD) owing to wave–wave interactions or by ion–neutral damping (IND) as a result of momentum exchange between ions and neutrals as a consequence of the charge exchange process. Because we are dealing with non-isolated clumps, we should also account for the typical time-scale of the system. Indeed, if the age of the clump is less than the time for damping to be effective, then waves can grow freely for a time-scale equal to the clump age.

The dominant mechanism of wave damping in the clump magnetic skin is NLD, because we assume the plasma to be completely ionized. Its damping rate can be expressed as (see Ptuskin & Zirakashvili 2003)

$$\Gamma_{\text{D}}(k) = \Gamma_{\text{NLD}}(k) = (2c_k)^{-3/2} k v_A \sqrt{\mathcal{F}(k)}, \quad (16)$$

where $c_k = 3.6$. In stationary conditions (when the system age is not a limiting factor), the wave growth rate (resulting from the streaming instability) equals the damping rate, as $\Gamma_{\text{CR}} = \Gamma_{\text{D}}$. Equating equation (15) to equation (16), the power in the resonant turbulent momentum results in

$$\mathcal{F} = \left[\frac{16}{3} \frac{\pi^2}{B_0^2} \left(p^4 v(p) \frac{\partial f}{\partial r} \right)_{p=p_{\text{res}}} r_L \right]^{2/3} 2c_k. \quad (17)$$

We recall that, in equation (17), the CR density gradient is computed within the clump skin, along the radial dimension. We need to verify whether the stationarity assumption is correct or not. Once

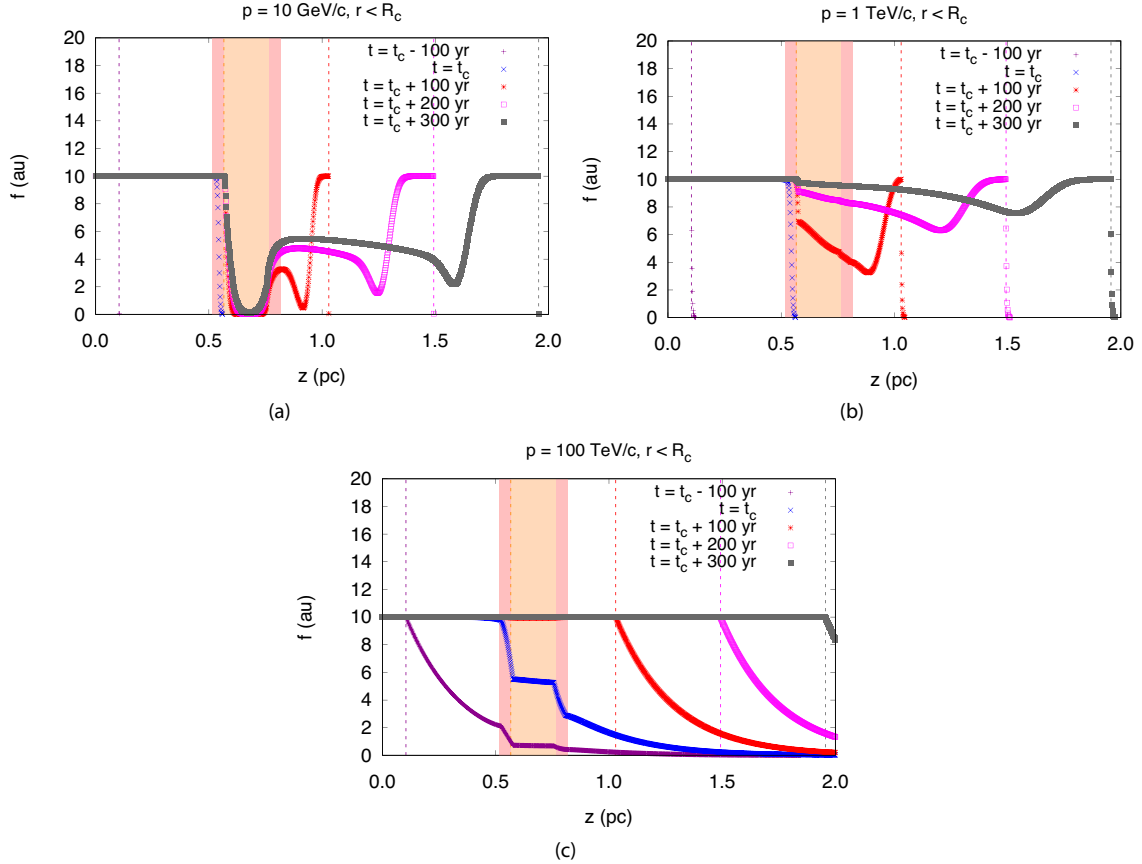


Figure 5. Density profiles of the accelerated particle in the shock region along z (at fixed radial position inside the clump) for CR protons of momentum (a) 10 GeV/c, (b) 1 TeV/c and (c) 100 TeV/c. Vertical dashed lines represent the shock position at a given time, as indicated in the legend. The light pink band defines the clump interior, while the dark pink band defines its magnetic skin.

we insert equation (17) into equation (16), setting v_A in $B_0 = 10\mu\text{G}$ and a typical ion density for a clump of $n_i = 10^{-4}n_c = 10^{-1}\text{ ion cm}^{-3}$, we find that stationarity is not valid for CR momenta larger than $p \geq 1\text{ TeV}/c$, where the clump age constrains the damping mechanism. Therefore, in this case, the power in the turbulence is computed by equating the growth rate of the MHD waves, as reported in equation (15), to the inverse of the clump age. This gives

$$\mathcal{F} = \frac{16}{3}\pi^2 \frac{v_A}{B_0^2} \left[p^4 v(p) \frac{\partial f}{\partial r} \right]_{p=p_{\text{res}}} \tau_{\text{age}}. \quad (18)$$

The result of this computation is shown in Fig. 7(a). The turbulence is generated in the clump magnetic skin, such that CRs with momentum between 100 GeV/c and 1 TeV/c are closer to the Bohm diffusive regime.

In contrast, in the clump interior, where neutral particles are abundant, the most efficient damping mechanism is IND (see Zweibel & Shull 1982 and Nava et al. 2016). Waves dissipate energy because of the viscosity produced in the charge exchange between ions and neutrals, such that previous neutrals start to oscillate with the waves. The frequency of ion–neutral collisions is (Kulsrud & Cesarsky 1971; Drury, Duffy & Kirk 1996)

$$\nu_c = n_n(\sigma v) = 8.4 \times 10^{-9} \left(\frac{n_n}{1\text{ cm}^{-3}} \right) \left(\frac{T_c}{10^4\text{ K}} \right)^{0.4}, \quad (19)$$

where an average over thermal velocities is considered. The rate of IND depends on the wave-frequency regime, namely whether ions and neutrals are strongly coupled or not. Defining the wave pulsation $\omega_k = kv_A$ in a collision-free medium, a study of the dispersion relationship defines different regimes for ion–neutral coupling, depending on the value of the ion-to-neutral density ratio defined in equation (1). These regimes are as follows.

i) If $\epsilon < 1/8$, there is a range of ω_k for which waves cannot propagate, that is, a range of k for which ω_k is a purely imaginary number. This range is for

$$4\epsilon < \frac{\omega_k^2}{v_c^2} < \frac{1}{4}, \quad (20)$$

which, within our assumptions ($\epsilon = 1.5 \times 10^{-3}$), equals the CR momenta in $15\text{ GeV}/c < p < 95\text{ GeV}/c$.

ii) In the intervals $\epsilon \ll 1$ and $(\omega_k/v_c)^2 \ll 4\epsilon$, then

$$\Gamma_{\text{IND}}(k) = -\frac{\omega_k^2}{2\nu_c} = -\frac{k^2 v_A^2}{2\nu_c}. \quad (21)$$

iii) If $\epsilon \ll 1$ and $(\omega_k/v_c)^2 \ll 1/4$, then

$$\Gamma_{\text{IND}} = -\frac{\nu_c}{2}. \quad (22)$$

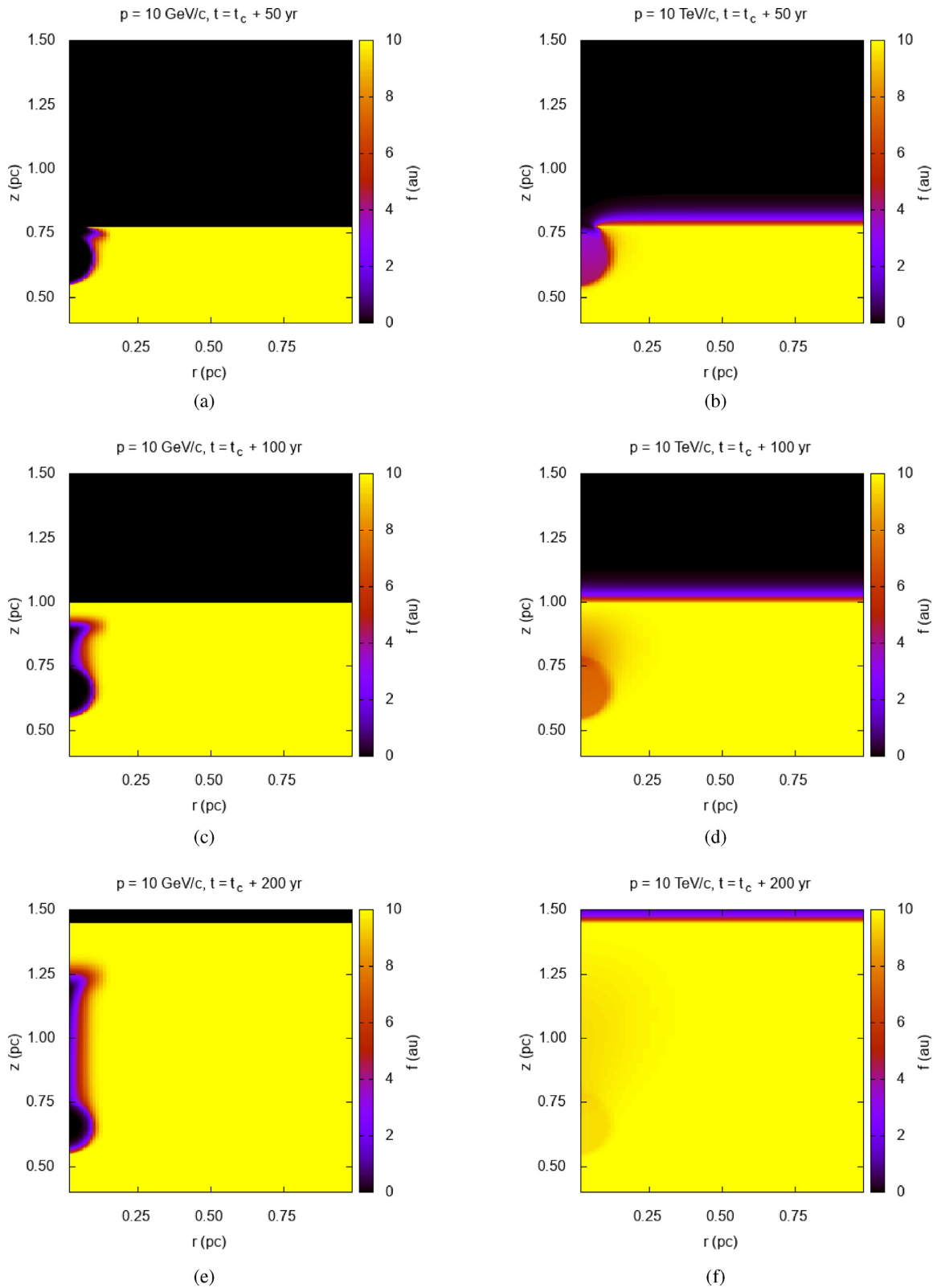


Figure 6. Distribution function of CR protons of momentum (a, c, e) 10 GeV/c and (b, d, f) 10 TeV/c at different times with respect to t_c : panels (a) and (b) are for $t = t_c + 50$ yr, (c) and (d) are for $t = t_c + 100$ yr, while (e) and (f) are for $t = t_c + 200$ yr. The precursor presence in front of the shock is clearly visible at 10 TeV.

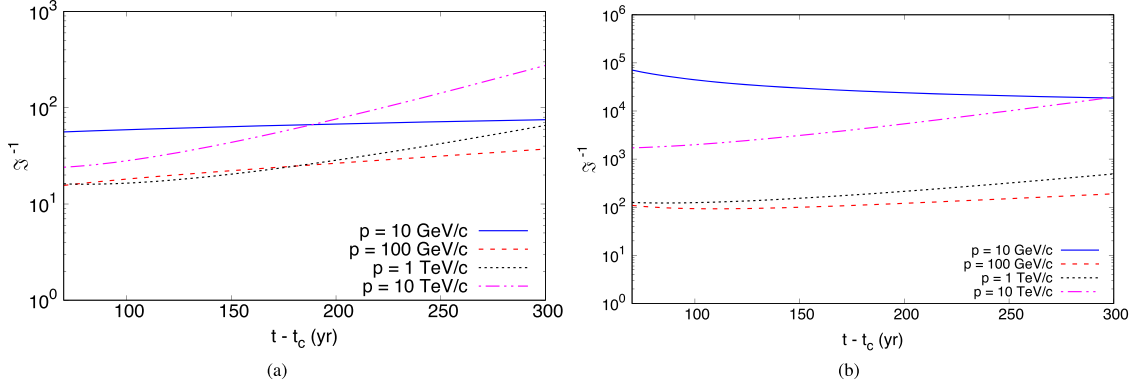


Figure 7. Ratio between the self-generated diffusion coefficient D_{self} and the Bohm diffusion coefficient D_{Bohm} , as a function of the clump age for different particle momenta (from equation (11), it follows that $\mathcal{F}^{-1} = (D_{\text{self}}/D_{\text{Bohm}})$). D_{self} is obtained by imposing $1/\Gamma_{\text{CR}} = \min(1/\Gamma_{\text{D}}, \tau_{\text{age}})$. (a) Results in the clump skin, where $\Gamma_{\text{D}} = \Gamma_{\text{NLD}}$ is considered; (b) results for the clump interior, where $\Gamma_{\text{D}} = \Gamma_{\text{IND}}$ is considered.

iv) If $\epsilon \gg 1$, then

$$\Gamma_{\text{IND}}(k) = -\frac{v_c}{2} \left[\frac{(\omega_k^2/v_c^2)}{(\omega_k^2/v_c^2) + \epsilon^2} \right]. \quad (23)$$

Again, the damping time Γ_{D}^{-1} should be compared with the clump age τ_{age} . For $p = 10$ GeV/c, the IND time is lower than the clump age, and therefore setting the equilibrium condition $\Gamma_{\text{D}} = \Gamma_{\text{IN}}$ through equation (22), we find

$$\mathcal{F} = \frac{16}{3} \pi^2 \frac{v_A}{B_0^2} \frac{2}{v_c} \left[p^4 v(p) \frac{\partial f}{\partial r} \right]_{p=p_{\text{res}}}. \quad (24)$$

For $p = 100$ GeV/c, the dominant damping mechanism is still IND. Setting the equilibrium condition $\Gamma_{\text{D}} = \Gamma_{\text{IN}}$ through equation (21), we obtain

$$\mathcal{F} = \frac{16}{3} \pi^2 \frac{1}{B_0^2} \left[p^4 v(p) \frac{\partial f}{\partial r} \right]_{p=p_{\text{res}}} \frac{2v_c}{k_{\text{res}}^2 v_A}. \quad (25)$$

On the other hand, for $p \geq 1$ TeV/c, the clump age is the limiting factor, because IN damping requires a longer time. As shown in Fig. 7(b), IND is mostly effective in damping waves resonant with CR particles of momentum lower than 10 GeV/c. Nonetheless, a strong suppression of the diffusion coefficient is reached between 100 GeV/c and 1 TeV/c.

3.3 Perpendicular diffusion

As shown in Fig. 3, the large-scale magnetic field is compressed and stretched around a large fraction of the clump surface. In this region, the Alfvénic turbulence produced by CR-driven instabilities is not sufficient to reach the Bohm limit because we have $\delta B_s \simeq (0.1-0.3)B_s$ at most, as shown in Fig. 7(a). As a consequence, if additional pre-existing turbulence is not amplified at the same level as the regular field, penetration into the clump requires perpendicular diffusion. According to quasi-linear theory, the diffusion perpendicular to the large-scale magnetic field, D_{\perp} , is related to parallel diffusion, D_{\parallel} , through (Casse, Lemoine & Pelletier 2002)

$$D_{\perp} = D_{\parallel} \frac{1}{1 + (\lambda_{\parallel}/r_L)^2}, \quad (26)$$

where λ_{\parallel} is the particle mean free path along the background field B_0 . Because $\lambda_{\parallel} = r_L(\delta B/B_0)^{-2}$, the perpendicular diffusion

coefficient results in

$$D_{\perp} = D_{\parallel} \frac{1}{1 + (\delta B/B_0)^{-4}}. \quad (27)$$

Hence, the radial diffusion into the clump is strongly suppressed with respect to the azimuthal diffusion along the field lines, provided that a tiny amplification of the magnetic field is realized. In the following, we assume that in the region downstream of the shock $(\delta B(k)/B)_{\text{down}} \simeq 1$ at all scales k resonant with accelerated particles. Our results from MHD simulations show that the magnetic field in the clump skin is amplified, reaching ~ 10 times the value in the unperturbed downstream, so that $B_s = 10B_{\text{down}}$ (Fig. 3). If the downstream pre-existing turbulence is amplified in the skin as well, then the Bohm diffusion limit can be reached: this is the case for isotropic diffusion, where the distinction between parallel and transverse diffusion is lost ($D_{\perp} = D_{\parallel}$) and a strong suppression of the diffusion coefficient is realized. However, if the turbulence in the clump skin remains at the same level as in the unperturbed downstream, then $(\delta B/B)_s \simeq 0.1$: this implies that, in the skin, parallel diffusion holds with $D_{\parallel s} = 10D_{\parallel \text{down}}$, while for perpendicular diffusion, using equation (27), we obtain $D_{\perp s} = 10^{-3}D_{\parallel \text{down}}$. Therefore, in this regime, particle penetration into the clump is even more suppressed than in the case of isotropic diffusion.

3.4 Proton spectrum

Once the proton distribution function is known from the solution of equation (6), it is possible to obtain the proton energy spectrum inside the clump, $J_c(p, t)$, at different times with respect to the first shock-clump contact, which we will denote as $t = t_c$. The average spectrum inside the clump reads as

$$J_c(p, t) = \frac{1}{V_c} \frac{d^3 N_c(t)}{dp^3}, \quad (28)$$

where $V_c = 4\pi R_c^3/3$ is the clump volume and $d^3 N_c(t)/dp^3$ is the number of protons inside the clump at a time t per unit volume in momentum space. The spectrum can be computed by summing all the discretized bins that define the clump volume. In this way, we obtain

$$J_c(p, t) = \frac{2\pi}{V_c} \sum_{i \in \text{clump}} f(r_i, z_i, p, t) r_i \Delta r_i \Delta z_i. \quad (29)$$

The results are shown in Fig. 8, where a proton cut-off momentum of

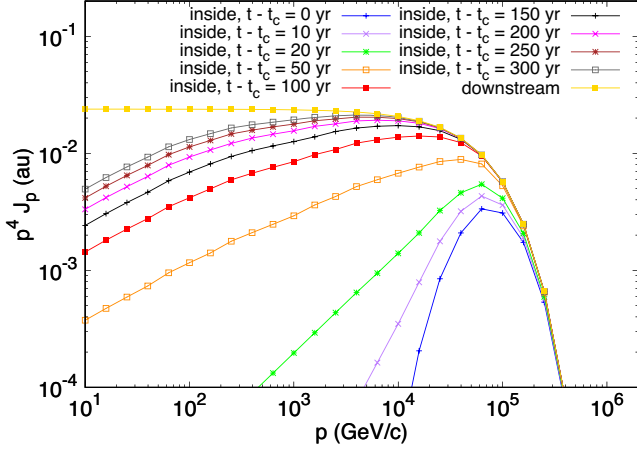


Figure 8. Proton spectrum inside clumps of different ages. The particle density in the downstream, which is constant in time, is also reported.

$p_{\text{cut}} = 70 \text{ TeV}/c$ was set in order to reproduce the very-high-energy gamma-ray data. Different proton spectra are expected at different times; in particular, for younger clumps the particle spectrum is much harder than the one accelerated at the shock as defined in equation (8). This is explained by the prevention of the penetration of low-energy CRs into the clump owing to the amplified magnetic field at the skin and because of the linear dependence of the diffusion coefficient on the particle momentum. In this way, the entrance of these particles into the clump is delayed. The spectral index of protons below $100 \text{ GeV}/c$ is as hard as $\alpha = -3.50$ when the clump age is 50 yr, moving to $\alpha = -3.54$ when the clump age is 150 yr, and finally to $\alpha = -3.57$ when the clump is 300 yr old. On the other hand, CRs with $p \gtrsim 100 \text{ TeV}/c$ are quite unaffected by the presence of the clump.

4 GAMMA-RAYS FROM A UNIFORM CLUMP DISTRIBUTION INSIDE THE SHELL

If the number of clumps is large enough, clumps could be the main source of gamma-ray emission, owing to hadronic inelastic collisions of CRs with the ambient matter. In such a case, the gamma-ray spectrum would reflect the spectrum of particles inside the clumps rather than that outside them, as produced by the shock acceleration. The effect of a clumpy environment on the time-dependent spectrum of gamma-rays from a SNR has also been investigated by Gaggero et al. (2018). In this section, we calculate the total gamma-ray spectrum resulting from hadronic interactions, assuming that clumps are uniformly distributed over the CSM where the shock expands. For the clump density that we assume here, the effect of a SNR shock impacting on a clump distribution can be described, with good accuracy, as the result of individual shock-clump interactions. Note that the average distance between clumps is much larger than the clump size and the simulation box.

The emissivity rate of gamma-rays from a single clump, given the differential flux of protons inside the clump $\phi_c(T_p, t)$ and the density of target material, is

$$\epsilon_c(E_\gamma, t) = 4\pi n_c \int dT_p \frac{d\sigma_{pp}}{dE_\gamma}(T_p, E_\gamma) \phi_c(T_p, t), \quad (30)$$

where $d\sigma_{pp}/dE_\gamma$ is the differential cross-section of the interaction, while $\phi_c(T_p, t)$ is obtained from the spectrum in equation (29), T_p being the particle kinetic energy. We used the analytical

parametrization for the p-p cross-section provided by the LIBPPGAM library (see Kafexhiu et al. 2016) and, specifically, we chose the parametrization resulting from the fit to SIBYLL 2.1.

In order to evaluate the cumulative distribution resulting from a fixed distribution of clumps, we need to include clumps that satisfy the following two conditions: (i) they should survive (not evaporate); (ii) they should be located between the position of the contact discontinuity (CD) R_{cd} and the shock position R_s . Indeed, we will assume that, once a clump passes through the CD, either it is destroyed by MHD instabilities or it is soon emptied of CRs. Therefore we should consider the minimum time between the evaporation time, τ_{ev} , and the time elapsed between the moment the clump crosses the forward shock and the moment it crosses the contact discontinuity τ_{cd} . As estimated in Section 2, the evaporation time is of the order of a few times the cloud crossing time (see equation 5). For the parameters we chose, this time is always greater than the SNR age. In the following, we will consider the conservative value of $\tau_{\text{ev}} = \tau_{\text{cc}}$. The CD radial position can be estimated by imposing that all the compressed matter is contained in a shell of size $\Delta R = R_{\text{SNR}} - R_{\text{cd}}$, so that

$$\frac{4}{3}\pi R_{\text{SNR}}^3 n_{\text{up}} = 4\pi R_{\text{SNR}}^2 \Delta R n_{\text{down}}, \quad (31)$$

which for a strong shock amounts to $\Delta R = R_{\text{SNR}}/12$. Therefore, the time that a clump takes to be completely engulfed in the CD is

$$\tau_{\text{cd}} = \frac{(2R_c + \Delta R)}{3v_s/4}. \quad (32)$$

The oldest clumps in the remnant shell will therefore have an age

$$T_{c,\text{max}} = \min(\tau_{\text{ev}}, \tau_{\text{cd}}). \quad (33)$$

In the following, we will consider a uniform spatial distribution of clumps, with number density $n_0 = 0.2 \text{ clumps pc}^{-3}$, inside the remnant of age T_{SNR} . Therefore, the total number of clumps at a distance between r and $r + dr$ from the source is equal to

$$\frac{dn(r)}{dr} = 4\pi n_0 r^2 \Rightarrow \frac{dn(t)}{dt} = 4\pi n_0 r^2(t) v_s(t). \quad (34)$$

Furthermore, we will assume a constant shock speed. We are interested in the number of clumps with a given age $t_{\text{age}}(r) = T_{\text{SNR}} - t_c(r)$. The number of clumps with an age between $t_{\text{age}} - \Delta t$ and t_{age} , namely $N(t_{\text{age}})$, is equal to the number of clumps that the shock has encountered between $T_{\text{SNR}} - t_{\text{age}}$ and $T_{\text{SNR}} - t_{\text{age}} + \Delta t$. It is equal to

$$N(t_{\text{age}}) = 4\pi n_0 \int_{T_{\text{SNR}} - t_{\text{age}}}^{T_{\text{SNR}} - t_{\text{age}} + \Delta t} r(t')^2 v_s(t') dt'. \quad (35)$$

The total number of clumps with $t_{\text{age}} \leq T_{c,\text{max}}$ is equal to $N_c \simeq 440$, which corresponds to the total mass in clumps inside the remnant shell, equal to $M_c \simeq 45M_\odot$. Consequently, the total gamma-ray emissivity due to these clumps is

$$\epsilon_c(E_\gamma, T_{\text{SNR}}) = \sum_{t_{\text{age}}=0}^{T_{c,\text{max}}} N(t_{\text{age}}) \epsilon_\gamma(E_\gamma, t_{\text{age}}). \quad (36)$$

We also account for the emissivity from the downstream region of the remnant, $\epsilon_{\text{down}}(E_\gamma)$, which is constant with time. The gas target in the downstream is considered to have an average density $\langle n_{\text{down}} \rangle$, which satisfies mass conservation in the whole remnant:

$$\frac{4}{3}\pi R_{\text{SNR}}^3 n_{\text{up}} = \frac{4}{3}\pi (R_{\text{SNR}}^3 - R_{\text{cd}}^3) \langle n_{\text{down}} \rangle. \quad (37)$$

Therefore we compute the gamma-ray flux from the source located at a distance d as

$$\phi_\gamma(E_\gamma, T_{\text{SNR}}) = \frac{1}{d^2} [V_c \epsilon_c(E_\gamma, T_{\text{SNR}}) + V_{\text{down}} \epsilon_{\text{down}}(E_\gamma)], \quad (38)$$

where $V_{\text{down}} = V_{\text{shell}} - N_c V_c$ and $V_{\text{shell}} = 4\pi(R_{\text{SNR}}^3 - R_{\text{cd}}^3)/3$.

5 APPLICATION TO RX J1713.7 – 3946

The Galactic SNR RX J1713.7 – 3946 (also called G347.3 – 0.5) represents one of the brightest TeV-emitters in the sky. The origin of its gamma-ray flux in the GeV–TeV domain (see Abdo et al. 2011 and Abdalla et al. 2016) has been the subject of long debate, because both hadronic and leptonic scenarios are able to reproduce, under certain circumstances, the observed spectral hardening. The presence of accelerated leptons is guaranteed by the detected X-ray shell (see Slane et al. 1999 and Tanaka et al. 2008), which shows a remarkable correlation with the TeV gamma-ray data, indicating a strong link between the physical processes responsible for these emission components. Meanwhile, a clear signature of accelerated hadrons, which would come from neutrinos, is still missing. RX J1713.7 – 3946 has been used as a standard candidate for the search of a neutrino signal from Galactic sources (Kappes et al. 2007; Villante & Vissani 2008; Morlino, Blasi & Amato 2009b). One of the arguments against the hadronic origin of the radiation that has been made is the absence of thermal X-ray lines (see Katz & Waxman 2008 and Ellison et al. 2010). In the scenario in which the remnant is expanding into a clumpy medium, the non-observation of thermal X-ray emission is naturally explained by the low-density plasma between clumps. On the other hand, because clumps remain mainly unshocked and therefore cold, they would not be able to emit thermal X-rays.

Clearly, the distribution of gas in RX J1713.7 – 3946 is crucial to establish the origin of the observed gamma-rays. The target material required by pp interactions may be present in any chemical form, including both the molecular and the atomic gas. High-resolution millimetre-wave observations of the interstellar CO molecules with the NANTEN telescope (Fukui et al. 2003) revealed the presence of molecular clouds in spatial correlation with TeV gamma-rays in the northwestern rim of the shell. The densest cores of such clouds have been detected in highly excited states of the molecular gas, manifesting signs of active star formation, including bipolar outflow and possibly embedded infrared sources (Sano et al. 2010). Other density tracers, such as cesium, have also confirmed the presence of very dense gas in the region ($n > 10^4 \text{ cm}^{-3}$), as indicated in a recent survey operated by the MOPRA telescope (Maxted et al. 2012). Furthermore, a combined analysis of CO and H I (Fukui et al. 2012) shows a counterpart of the southeastern rim of the gamma-ray data in atomic hydrogen. The multiwavelength observations point towards the clear presence of a non-homogeneous environment, where the young SNR is expanding.

The estimated distance of the remnant is about $d \simeq 1 \text{ kpc}$ (Fukui et al. 2003; Moriguchi et al. 2005), while the radial size of the detected gamma-ray shell today extends up to $R_s \simeq 0.6$ (Abdalla et al. 2016). The remnant is supposed to be associated with the Chinese-detected Type II SN explosion of AD 393 (Wang, Qu & Chen 1997); this would assign to the remnant an age of $T_{\text{SNR}} \simeq 1625 \text{ yr}$. The age, distance and detected size yield an average shock speed of about $\langle v_s \rangle \simeq 6.3 \times 10^8 \text{ cm s}^{-1}$. Measurements of the proper motion of X-ray structures indicate that the shock speed today should be $v_s \leq 4.5 \times 10^8 \text{ cm s}^{-1}$ (Uchiyama et al. 2007), meaning that the shock has slowed down slightly during its

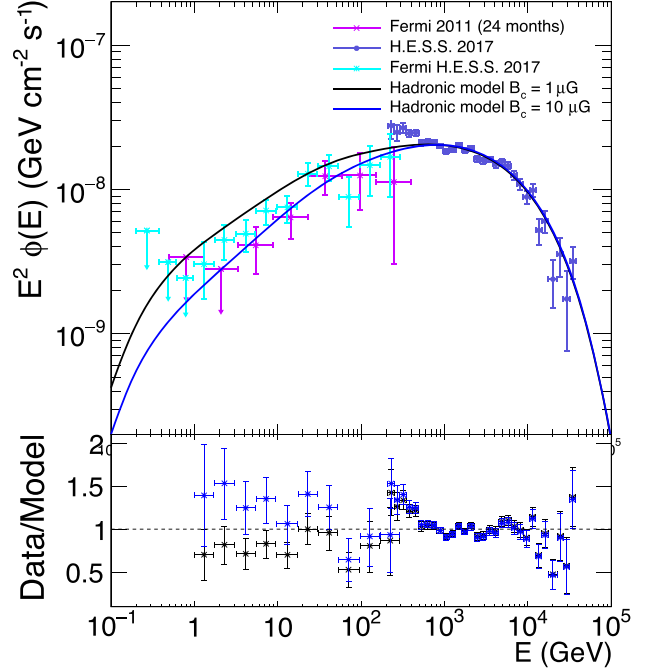


Figure 9. Gamma-ray flux from SNR RX J1713.7 – 3946. The points are *Fermi*-LAT data (pink), HESS data (violet) and HESS analysis of *Fermi*-LAT data (light blue). The hadronic models (solid lines) refer to the configuration with a magnetic field inside the clump equal to $B_c = 1 \mu\text{G}$ (black) and to $B_c = 10 \mu\text{G}$ (blue). The field in the clump skin is fixed to $B_s = 100 \mu\text{G}$ in both models.

expansion. This is expected in SNR evolution (Truelove & McKee 1999) during both the ejecta-dominated (ED) and the Sedov–Taylor (ST) phase. RX J1713.7 – 3946 is nowadays moving from the ED to the ST phase, and therefore we can safely assume a constant shock speed through the time evolution up to now, with a value of $v_s = 4.4 \times 10^8 \text{ cm s}^{-1}$ (Gabici & Aharonian 2014). At this speed, the time that the CD takes to completely engulf a clump is, from equation (32), $\tau_{\text{cd}} \simeq 300 \text{ yr}$. On the other hand, the evaporation time would be much longer, indicating that the relevant clumps contributing to the gamma-ray emission are younger than $T_{c, \text{max}} = 300 \text{ yr}$.

With the parameters representing RX J1713.7 – 3946 as defined above, we can compute the gamma-ray flux of the remnant shell through equation (30). We fix the normalization k of the resulting gamma-ray flux by minimizing the χ^2 of the data from the *Fermi*-LAT and the High Energy Stereoscopic System (HESS) with respect to our model. We investigate two different configurations. The first model explores a configuration with the magnetic field inside the clump reduced by a factor of 10 with respect to the CSM value, in order to account for the effect of IND, and therefore it is set to $B_c = 1 \mu\text{G}$. The second model, instead, explores the situation in which no IND is acting, and therefore the magnetic field inside the clump is set to be $B_c = 10 \mu\text{G}$, as in the CSM. The results are shown in Fig. 9. The GeV data from two years of data-taking with the *Fermi*-LAT satellite (Abdo et al. 2011) are reported, together with the HESS TeV data (Abdalla et al. 2016) and with the HESS Collaboration analysis of five years of *Fermi*-LAT data, as reported in Abdalla et al. (2016). The two models predict slightly different trends in the GeV emission of the remnant. A more pronounced hardening in the case of $B_c = 10 \mu\text{G}$ better reproduces the GeV data, while a flatter trend is visible in case diffusion would act

less efficiently inside the clump. In this respect, electrons are more suitable for deriving constraints on the magnetic field properties of the remnant. A more quantitative study on secondary electrons from pp interactions will be discussed elsewhere.

The normalization constant k , obtained by fitting the gamma-ray data, defines the amount of ram pressure $P_{\text{ram}} = \rho_{\text{up}} v_s^2$ that is instantaneously converted into CR pressure. The latter is defined, for relativistic particles, as

$$P_{\text{CR}} = \frac{k}{3} \int_{m_p c}^{\infty} 4\pi p^2 dp f_0(p) pc. \quad (39)$$

The efficiency of the pressure conversion mechanism from bulk motion to accelerated particles is equal to $\eta = P_{\text{CR}}/P_{\text{ram}} \simeq 2$ per cent. Such a value is somewhat smaller than the efficiency estimated by other works in the context of hadronic scenarios, where usually $\eta \simeq 10$ – 20 per cent (see e.g. G44; Gabici & Aharonian 2014). Compared with G44, the main differences are due to the higher total target mass we use here ($\sim 45M_{\odot}$ versus $\sim 15M_{\odot}$), which is close to the total mass in clumps estimated by HD simulations (Inoue et al. 2012). A weaker effect is also due to the fact that we are neglecting adiabatic losses, which leads to a smaller acceleration efficiency by a factor of less than 2. Furthermore, comparing our result with Gabici & Aharonian (2014), we should note a few more differences. We consider a constant shock speed and assume a αp^{-4} accelerated spectrum, while Gabici & Aharonian (2014) use a time-dependent shock velocity and a steeper acceleration spectrum $\alpha p^{-4.2}$. The latter assumption implies a number density of accelerated protons at 100 TeV smaller by a factor of ~ 10 (for the given acceleration efficiency). For this reason, Gabici & Aharonian (2014) adopted a larger target mass in clumps, $\sim 500M_{\odot}$.

5.1 Observing clumps through molecular lines

An interesting possibility to detect clumps is provided by radio observations. Secondary electrons emit synchrotron radiation in the radio domain. On top of this continuum, the molecular gas emits lines. For instance, rotational CO lines are often observed in these systems (Fukui et al. 2003). In the case of RX J1713.7–3946, a few-arcsecond angular resolution is needed to probe the spatial scales of clumps: such a small scale can currently be achieved only through the superior angular resolution of the Atacama Large Millimeter Array (ALMA). A precise pointing is, however, required, because the instrument field of view of ≤ 35 arcsec would not entirely cover a region as extended as the remnant RX J1713.7–3946.

In the following, we will evaluate the radio flux for the $J = 1 \rightarrow 0$ rotational line of the CO molecule. This transition is located at $\nu = 115$ GHz (band 3 of ALMA receivers) and radiates photons at a rate equal to $A_{10} = 6.78 \times 10^{-8}$ Hz. Assuming a CO abundance of $n_{\text{CO}}/n_c = 7 \times 10^{-5}$ and a clump density of $n_c = 10^3 \text{ cm}^{-3}$, the expected flux from an individual clump amounts to

$$F = \frac{hA_{10}}{4\pi d^2} N_{\text{CO}} = 3.15 \times 10^{-3} \text{ Jy}, \quad (40)$$

where h is the Planck constant and N_{CO} is the number of CO molecules contained in each clump ($d = 1$ kpc is assumed). The flux level obtained in equation (40) is well within the performance of the nominal ten 7-m-diameter antennas configuration of the ALMA observatory. In this respect, CO line measurements constitute a powerful tool to constrain the density of individual clumps located in the remnant environment.

Finally, a well-known shock-tracer into molecular clouds is the SiO molecule. Si ions are generally contained in dust grains, which

are destroyed by the passage of a shock, and can form SiO in the gas phase (Gusdorf et al. 2008a,b). This tracer has been successfully used for the SNR W 51C (Dumas et al. 2014). In the case of RX J1713.7–3946, existing observations towards the northwest rim, in the so-called Core C, do not show evidence for a significant amount of SiO emission (Maxted et al. 2012). This result can be interpreted in a variety of ways: either Core C is located outside the remnant or, if it is inside, the shock has not yet penetrated into the densest cores where dust grains are typically located. A further possibility is that the shock propagating inside the core is not strong enough to sputter Si ions efficiently from the grains. Indeed, Gusdorf et al. (2008a) showed that a shock velocity $\gtrsim 25 \text{ km s}^{-1}$ is necessary for an efficient sputtering, and the shock speed inside the clump could be lower than such a threshold if $\chi \gtrsim 10^5$ (see equation 4). As a consequence, a positive SiO detection could shed light on the value of the density contrast χ .

5.2 Clumps and the X-ray variability

The origin of bright hotspots in the non-thermal X-ray image of RX J1713.7–3946 (Uchiyama et al. 2007), decaying on the time-scale of 1 yr, remains an unexplained puzzle. Several time-variable compact features have been identified in the *Chandra* data, mostly in the northwest part of the shell. The size of the fast-variable X-ray hotspots in RX J1713.7–3946 is about $\theta \simeq 20$ arcsec, which corresponds to a linear size of $L_x = d\theta \simeq 3 \times 10^{17} \text{ cm}$ at a distance $d \simeq 1$ kpc. Similar time-dependent features have also been identified in the young SNRs Cas A (Uchiyama & Aharonian 2008; Sato et al. 2018; Fraschetti 2018) and G 330.2+1.0 (Borowsky 2018). It has already been suggested that the X-ray variability could be connected to the clump scenario applied at the forward shock (Inoue et al. 2012) or, for the case of Cas A, even at the inward shocks, originating as a reflection from the collision between the forward shock and overdense clumps (Fraschetti 2018). The striking similarity between the physical size of the observed hotspots and the MHD instabilities that are formed in shock flows around clumpy structures suggests a possible intrinsic physical link.

In the context of shock propagation into a non-uniform, ambient medium, as discussed above, a natural interpretation of the X-ray variability seems to be electron synchrotron cooling in the amplified large-scale magnetic field. It was shown in Fig. 3 that the spatial scale at which amplification takes place is of the order of the clump size. The time-scale over which electrons of energy E lose energy is $t_{\text{synch}} \simeq 12.5(B/\text{mG})^{-2}(E/\text{TeV})^{-1} \text{ yr}$. The typical energy of synchrotron photons is $E_{\text{synch}} = 0.04(B/\text{mG})(E/\text{TeV})^2 \text{ keV}$, and hence the energy-loss time-scale at the observed frequency is

$$t_{\text{synch}} \simeq 2.4 \left(\frac{B}{\text{mG}} \right)^{-3/2} \left(\frac{E_{\text{syn}}}{\text{keV}} \right)^{-1/2} \text{ yr}. \quad (41)$$

For a density contrast of $\chi = 10^5$ (see equation 3), our MHD simulation shows that the amplification of the magnetic field can bring the background field up to 10 times above the downstream value. Hence the milligauss magnetic field needed to explain the observed timescale would require a downstream magnetic field of $\sim 100 \mu\text{G}$.

5.3 Resolving the gamma-ray emission

Deep morphological and spectroscopic studies of SNRs are among the highest-priority scientific goals of the forthcoming Cherenkov

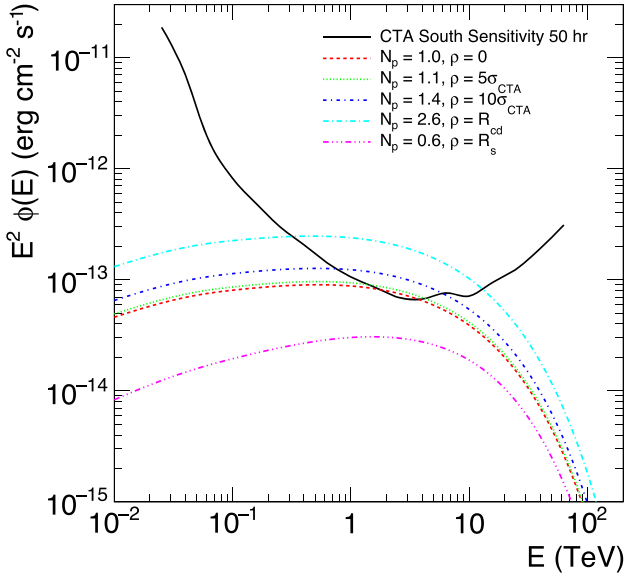


Figure 10. CTA Southern Array sensitivity curve for point-like sources located in the FoV centre (zenith $\theta = 20^\circ$, pointing average) for an observation time equal to 50 hr (black solid line). Also shown are the gamma-ray fluxes resulting from the overlapping clumps (indicated in the legend) in different circular sky regions of radius σ_{CTA} , located at a distance ρ from the SNR centre.

telescope array (CTA) (Actis et al. 2011; Acero et al. 2017). Despite its great potential, CTA will be not able to resolve the gamma-ray emission from individual clumps. For a SNR at a distance of 1 kpc, the angular extension of a clump with a typical size of ~ 0.1 pc does not exceed 20 arcsec, which is one order of magnitude smaller than the angular resolution of CTA. Nevertheless, the component related to the superposition of gamma-ray emission of several clumps within the instrument point spread function (PSF) could in principle be detected. Hence, we estimate the number of clumps $dN_p/d\rho$ that overlap along the line of sight l , when observing a disc-like region with radius equal to the instrument PSF centred at a distance $\rho = \sqrt{r^2 - l^2}$ from the centre of the SNR. Assuming a uniform distribution of clumps, as described in Section 4, and integrating it along the line of sight, we obtain

$$\frac{dN_p}{d\rho}(\rho) = 2n_0 \left(\sqrt{R_s^2 - \rho^2} - \max \left[0, \sqrt{R_{\text{cd}}^2 - \rho^2} \right] \right), \quad (42)$$

where the emission is assumed to come from the shocked ISM located between the contact discontinuity and the forward shock (Morlino & Caprioli 2012). Considering a uniform map of the whole remnant by CTA,² we compute the gamma-ray flux from several circular regions centred at a given ρ and with radius equal to $\sigma_{\text{CTA}} = 0.037$ (at $E_\gamma = 10$ TeV) (Acharya et al. 2017). We considered ρ spanning from 0 to R_s . Moreover, we should take into account the different ages of clumps, because they produce gamma-rays with different spectral shapes, as shown in Section 3.4. These fluxes are represented in Fig. 10, which also shows the sensitivity curve of the CTA Southern Array, for a 50-hr observation of a point-like source centred in the instrument field of view (FoV). The predicted flux clearly shows that CTA will be able to resolve the gamma-ray

emission from clumps contained in a circle of radius equal to its high-energy PSF over about one decade in energy. However, the gamma-ray fluxes expected in different pointing regions strongly reflect the number of overlapping clumps, which represent the main contributors to the emission. Such a number is maximum when $\rho = R_{\text{cd}}$, where $N_p = 2.6$. Given the limited number of overlapping clumps in each pointing region, large fluctuations are expected, according to the Poissonian statistics. Therefore, the detection of such fluctuations constitutes a characteristic signature of the presence of clumps. The magnitude of the fluctuations depends on the clump density n_0 in the CSM. In fact, once the mass of the target gas is fixed, more massive clumps with $n_c = 10^4 \text{ cm}^{-3}$ would require a lower clump density and therefore would produce much stronger fluctuations on the scale of σ_{CTA} . These types of morphological studies are hence crucial to deriving constraints on the number density of clumps in the remnant region. Large fluctuations on the scale of σ_{CTA} are not expected if the SNR is expanding into a uniform medium or into a medium where the density contrast is such that the clump evaporates soon after the shock crossing, namely if $\tau_{\text{ev}} \ll T_{\text{SNR}}$. The latter condition can be rearranged using equations (4) and (5) to give an upper limit for the density contrast that reads $\chi \ll (T_{\text{SNR}} v_s / 2R_c)^2 \simeq 10^3 (R_c / 0.1 \text{ pc})^{-2}$. Such a small density contrast also implies a smaller amplified magnetic field and, as a consequence, a flattening of the gamma-ray spectrum.

6 CONCLUSIONS

The presence of inhomogeneities in the CSM, in the form of dense molecular clumps where a shock propagates, strongly affects the plasma properties, in such a way that the large-scale magnetic field around the clumps is amplified. As a consequence, the propagation of particles accelerated at the shock proceeds in such a way that low-energy particles need more time to penetrate the clump compared with high-energy ones. The resulting energy spectrum of particles inside the clump is significantly harder than the spectrum accelerated at the shock through DSA. Such a scenario is very common in the case of core-collapse SNe, where the remnant typically expands in a region populated by dense molecular clouds. It is thus necessary to account for the inhomogeneous CSM to correctly predict the gamma-ray spectrum from the SNRs. In this work, we numerically solved the propagation of accelerated particles in the shock region in the presence of clumps, taking into account the magnetic field amplification produced by both the field compression and the shear motion, and its effect on the particle diffusion. The most important parameter in this scenario is the density contrast between the diffuse CSM and the clumps. Using MHD simulations, we showed that the magnetic amplification is effective only when the density contrast is larger than 10^3 .

Given that clumps contain most of the target gas, the gamma-ray spectrum produced in hadronic collisions of accelerated particles appears to be much harder than the parent spectrum. We demonstrated this effect for the brightest SNR in TeV gamma-rays, RX J1713.7 – 3946. The cumulative contribution of clumps embedded between the contact discontinuity and the current shock position is able to reproduce the observed GeV hardening, although some degeneracy in the parameter space of the model is present. Remarkably, for the gas density inside the clump assumed here ($n_c = 10^3 \text{ cm}^{-3}$), the evaporation time is much longer than the SNR age. As a consequence, the clumps crossed by the forward shock do not produce significant thermal X-ray emission, in agreement with observations. We argue that such a scenario can naturally account

²<http://www.cta-observatory.org/science/cta-performance/>

for the fast variability in non-thermal X-rays reported in some hotspots inside RX J1713.7 – 3946, thanks to the magnetic field being amplified around the clumps. The electrons entering these regions rapidly lose their energy because of synchrotron emission. An independent signature of the ‘clump’ origin of the gamma-ray emission could be revealed from a morphological study performed with the next-generation, ground-based, gamma-ray observatory CTA. The superb sensitivity and the high angular resolution of CTA could allow the resolution of small regions that contains only few clumps. In these regions we do expect a large spatial fluctuation of the gamma-ray flux, unlike a scenario where the SNR is expanding into a uniform medium.

ACKNOWLEDGEMENTS

We acknowledge the authors of the PLUTO code (Mignone et al. 2007) that was used in this work to model the shock–clump MHD interaction. This research also made use of the CTA instrument response functions (prod3b-v1), as released by the CTA Consortium and Observatory. SG acknowledges support from Agence Nationale de la Recherche (grant ANR- 17-CE31-0014) and from the Observatory of Paris (Action Fédératrice CTA).

REFERENCES

Abdalla H., HESS Collaboration et al., 2016, *A&A*, 612, 6
 Abdo A. A., Fermi LAT Collaboration et al., 2011, *AJ*, 734, 28
 Acero F., CTA Consortium et al., 2017, *AJ*, 840, 74
 Acharya B. S., CTA Consortium et al., 2019, *Science with the Cherenkov Telescope Array*
 Ackermann M., Fermi LAT Collaboration et al., 2013, *Science*, 339, 807
 Actis M., CTA Consortium et al., 2011, *Exp. Astron.*, 32, 193
 Bell A. R., 1978, *MNRAS*, 182, 147
 Berezhko E. G., Ksenofontov L. T., Völk H. J., 2013, *ApJ*, 763, 14B
 Blandford R. D., Ostriker J. P., 1978, *ApJ*, 221, L29
 Borkowski K. J., Reynolds S. P., Williams B. J., Petre R., 2018, *ApJ*, 868, L21
 Cardillo M., Amato E., Blasi P., 2016, *A&A*, 595A, 58C
 Casse F., Lemoine M., Pelletier G., 2002, *Phys. Rev. D*, 65, 023002
 Chevalier R. A., 1999, *ApJ*, 511, 798
 Drury L. O’C., 1983, *Rep. Prog. Phys.*, 46, 973
 Drury L. O’C., Duffy P., Kirk J. G., 1996, *A&A*, 309, 1002
 Dumas G., Vaupré S., Ceccarelli C., Hily-Blant P., Dubus G., Montmerle T., Gabici S., 2014, *ApJ*, 786, L24
 Dwarkadas V. V., 2007, *ApJ*, 667, 226
 Ellison D. C., Patnaude D. J., Slane P., Raymond J., 2010, *ApJ*, 712, 287
 Frascchetti F., 2013, *ApJ*, 770, 84
 Frascchetti F., Katsuda S., Sato T., Jokipii J. R., Giacalone J., 2018, *Phys. Rev. Lett.*, 120, 251101
 Fukui Y. et al., 2003, *Pub. Astron. Soc. J.*, 55, L61
 Fukui Y. et al., 2012, *ApJ*, 746, 82
 Gabici S., Aharonian F. A., 2014, *MNRAS*, 455, L70
 Gabici S., Aharonian F. A., 2016, *EPJ Web Conf.*, 121, 04001
 Gabici S., Montmerle T., 2016, *PoS ICRC2015*, 34, 29

Gaggero D., Zandanel F., Cristofari P., Gabici S., 2018, *MNRAS*, 475, 5237G
 Giacalone J., Jokipii J., 2007, *ApJ*, 663, L41
 Ginzburg V. L., Syrovatsky S. I., 1961, *Progr. Theor. Phys. Suppl.*, 20, 1
 Gusdorf A., Cabrit S., Flower D. R., Pineau Des Forêts G., 2008, *A&A*, 482, 809
 Gusdorf A., Pineau Des Forêts G., Cabrit S., Flower D. R., 2008, *A&A*, 490, 695
 Hennebelle P., 2013, *New Trends Radio Astron. ALMA Era*, 476, 115
 Inoue T., Yamazaki R., Inutsuka S., Fukui Y., 2012, *ApJ*, 744, 71
 Jones T. W., Ryu D., Tregillis I. L., 1996, *ApJ*, 473, 365
 Kafexhiu E., Aharonian F. A., Taylor A. M., Vila G. S., 2014, *Phys. Rev. D*, 90, 12
 Kappes A., Hinton J., Stegmann C., Aharonian F. A., 2007, *ApJ*, 656, 870
 Katz B., Waxman E., 2008, *J. Cosm. Astropart. Phys.*, 01, 018
 Klein R. I., McKee C. F., Colella P., 1994, *ApJ*, 420, 213
 Kulsrud R. M., Cesarsky C. J., 1971, *ApJ*, 8, L189
 Mac Low M.-M., McKee C. F., Klein R. I., Stone J. M., Norman M. L., 1994, *ApJ*, 433, 757
 Maxted N. I. et al., 2012, *MNRAS*, 422, 2230
 Mignone A., Bodo G., Massaglia S., Matsakos T., Tesileanu O., Zanni C., Ferrari A., 2007, *ApJS*, 170, 1
 Moriguchi Y., Tamura K., Tawara Y., Sasago H., Yamaoka K., Onishi T., Fukui Y., 2005, *ApJ*, 631, 947
 Morlino G., Caprioli D., 2012, *A&A*, 538, 15
 Morlino G., Amato E., Blasi P., 2009a, *MNRAS*, 392, 240
 Morlino G., Blasi P., Amato E., 2009b, *Astropart. Phys.*, 31, 376
 Nava L., Gabici S., Marcowith A., Morlino G., Ptuskin V. S., 2016, *MNRAS*, 461, 4
 Orlando S., Peres G., Reale F., Bocchino F., Rosner R., Plewa T., Siegel A., 2005, *A&A*, 444, 505
 Orlando S., Bocchino F., Reale F., Peres G., Pagano P., 2008, *ApJ*, 678, 274
 Padovani M., Galli D., Glassgold A. E., 2009, *A&A*, 501, 619
 Phan V. H. M., Morlino G., Gabici S., 2018, *MNRAS*, 480, 5167
 Ptuskin V. S., Zirakashvili V. N., 2003, *A&A*, 403, 1
 Sano H. et al., 2010, *ApJ*, 724, 1
 Sano T., Nishihara K., Matsuoka C., Inoue T., 2012, *ApJ*, 758, 126
 Sato T., Katsuda S., Morii M., Bamba A., Hughes J. P., Maeda Y., Ishida M., Frascchetti F., 2018, *ApJ*, 853, 46
 Skilling J., 1971, *ApJ*, 170, 265
 Skilling J., 1975, *MNRAS*, 172, 557
 Slane P., Gaensler B. M., Dame T. M., Hughes J. P., Plucinsky P. P., Green A., 1999, *ApJ*, 525, 357
 Tanaka T. et al., 2008, *ApJ*, 685, 988
 Truelove J. K., McKee C. F., 1999, *ApJS*, 120, 2
 Uchiyama Y., Aharonian F. A., 2008, *ApJ*, 667, L105
 Uchiyama Y., Aharonian F. A., Tanaka T., Takahashi T., Maeda Y., 2007, *Nature*, 449, 7162
 Villante F., Vissani F., 2008, *Phys. Rev. D*, 78, 103007
 Wang Z. R., Qu Q. Y., Chen Y., 1997, *A&A*, 318, L59
 Zirakashvili V. N., Aharonian F. A., 2010, *ApJ*, 708, 2
 Zweibel E. G., Shull J. M., 1982, *ApJ*, 259, 859

This paper has been typeset from a $\text{\TeX}/\text{\LaTeX}$ file prepared by the author.